Nematic-Smectic Transition in Spherical Shells

Teresa Lopez-Leon,[1,2,*] Alberto Fernandez-Nieves,[3] Maurizio Nobili,[1,2] and Christophe Blanc[1,2]

[1]*Université Montpellier 2, Laboratoire Charles Coulomb UMR 5221, F-34095, Montpellier, France*

[2]*CNRS, Laboratoire Charles Coulomb UMR 5221, F-34095, Montpellier, France*

[3]*Georgia Institute of Technology, School of Physics, 837 State St. NW, Atlanta, Georgia 30332, USA*

(Received 11 March 2011; published 15 June 2011)

We study the nematic-smectic phase transition of a thermotropic liquid crystal confined to a spherical shell. Far from the nematic-smectic phase transition temperature, T_{NS}, we observe a configuration with four $+1/2$ defects, as predicted by theory. Since in this case $K_1 \approx K_3$, the four defects are confined at the thinnest part of the shell to minimize the energy associated with the defect cores. By contrast, near T_{NS}, where $K_3 \gg K_1$, bend distortions become prohibited and the defects organize themselves along a great circle of the sphere, confirming recent theoretical and simulation results. During this structural change, the defects associate in two pairs that behave independently. In the smectic phase, we observe a new configuration displaying curvature walls.

DOI: 10.1103/PhysRevLett.106.247802 PACS numbers: 61.30.Jf, 61.30.Hn, 64.75.Xc

Nematic liquid crystals are typically formed by rodlike molecules displaying orientational order along an average direction, **n**, called the director. When a nematic is confined to a spherical shell, the director field is necessarily disrupted by the presence of topological defects [1,2]. These systems not only are rich systems to study topological problems, but they also provide a promising route for generating colloids with a valence [3], which is an important goal in material science [4]. Different defect structures have been observed, differing in the number and distribution of defects [5]. The associated elastic energy is given by the Franck-Oseen free energy density [6]:

$$f = \frac{1}{2}K_1(\nabla \cdot \mathbf{n})^2 + \frac{1}{2}K_2(\mathbf{n} \cdot \nabla \times \mathbf{n})^2 + \frac{1}{2}K_3(\mathbf{n} \times \nabla \times \mathbf{n})^2 \quad (1)$$

where K_1 and K_3 are the elastic constants associated to splay and bend distortions. In the limit of a very thin shell, the director can be regarded as a surface field, and thus, the twist term associated to K_2 can be neglected. When $K_1 = K_3$, theory predicts a configuration with four defects arranged in a tetrahedral fashion [7], as shown in Fig. 1(a). In this configuration, each defect has a topological charge $s = +\frac{1}{2}$, reflecting the π rotation experienced by **n** along a path encircling each defect. This is consistent with a mathematical theorem due to Poincaré and Hopf, which establishes that the total topological charge for a nematic sphere is $s = +2$ [8]. Interestingly, a new arrangement is expected when $K_3 \gg K_1$, in which the four $s = +\frac{1}{2}$ defects are placed along a great circle of the sphere [9,10], as shown in Fig. 1(b). These theoretical expectations, however, have never been experimentally tested nor has the effect of the anisotropy in the elastic constants been experimentally explored.

In this Letter, we study the effect of the anisotropy in elastic constants K_1 and K_3 by taking advantage of the divergence of K_3 near the nematic-smectic phase transition temperature, T_{NS} [11]. Because of the heterogeneous thickness of the experimental shells, the four $s = +\frac{1}{2}$ defects characteristic of the nematic phase appear confined in a small region of the shell and not arranged in a tetrahedral configuration. By decreasing the temperature toward T_{NS}, the defects progressively separate to eventually arrange themselves in a great circle. Below T_{NS}, the translational symmetry of the nematic phase is broken and a smectic shell is formed.

To fabricate the liquid crystal shells, we generate double emulsions in a microfluidic glass capillary device [12]. An inner aqueous droplet is encapsulated inside an outer liquid crystal droplet, as schematically shown in Fig. 1(c), which is in turn dispersed in a continuous aqueous phase. The average thickness of the shell, h, is given by the difference between the outer and inner radii, $R - a$. In our experiments, R is within the (30–120) μm range and h is typically 2%–3% of R. The inner and outer phases contain 1 wt % of polyvinyl alcohol (PVA, $M_w \sim 20.000$ g mol^{-1}), which stabilizes the double emulsion and imposes planar

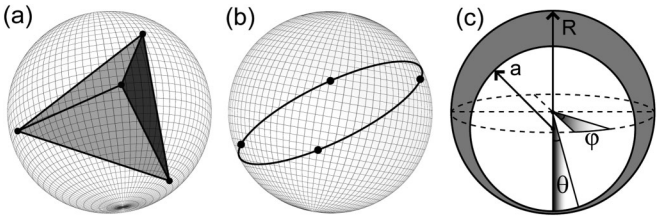

FIG. 1. Arrangement of four $s = +\frac{1}{2}$ disclinations on a bidimensional shell (a) in a tetrahedral configuration when $K_1 \approx K_3$, and (b) along a great circle when $K_1 \ll K_3$. (c) Cross section of an experimental shell with nonuniform thickness.

degenerate anchoring to the liquid crystal. The middle phase is 4-*n*-octyl-4-cyanobiphenyl (8CB), a liquid crystal displaying a nematic-smectic phase transition at $T_{NS} = 33.5\,^{\circ}\mathrm{C}$. Since the inner aqueous solution is slightly denser than 8CB, the inner droplet sinks inside the outer one, making the shell thinner at the bottom and thicker at the top. In terms of thickness, the experimental shells are, thus, axisymmetric with respect to the gravity direction, with a nonuniform thickness $\delta \approx h(1 - \cos\theta)$ that depends on the zenithal angle θ [Fig. 1(c)]. We fabricate and store the shells at 37 °C, where 8CB is in the nematic phase. Because of the divergence of K_3 at T_{NS}, an accurate control of temperature is required to guarantee a quasistatic approach to the nematic-smectic phase transition; we use a heating stage with a Lakeshore controller to regulate the temperature with a precision of 0.01 °C. Additionally, after changing temperature, we wait for 20 minutes to ensure that the system is indeed in an equilibrium state.

Figures 2(a)–2(g) show the birefringence texture of a nematic shell with four defects as the temperature T is quasistatically decreased toward T_{NS}. The evolution of the defect positions and director fields is represented in Figs. 2(h)–2(k). When $T - T_{NS} \gtrsim 1\,^{\circ}\mathrm{C}$, the four defects appear confined at the bottom of the shell, as shown in Fig. 2(a). However, as T approaches T_{NS}, defects 1 and 2 start moving away from each other, while defects 3 and 4 only slightly increase their separation, as shown in Figs. 2(a)–2(d). It is only after defects 1 and 2 reach the equatorial plane that defects 3 and 4 significantly move away from each other to eventually reach the equatorial plane too, as shown in Figs. 2(e)–2(g). To quantify the evolution of the defect pairs, we plot the ratio between the angles subtended by defects 1-2 and 3-4 with respect to the center of the shell, α_{12} and α_{34}, as a function of $T - T_{NS}$. When T is far from T_{NS}, the defects are almost located at the vertices of a square and $\alpha_{12} \approx \alpha_{34}$, as shown in Fig. 3. Decreasing T causes the elongation of the structure into a rhombus with $\alpha_{12} > \alpha_{34}$. This elongation becomes maximum at $T - T_{NS} = 0.06$. Below this, defects 3-4 progressively migrate toward the equatorial plane. As a result, α_{12}/α_{34} decreases until eventually the defects are located in a great circle and $\alpha_{12} \approx \alpha_{34}$ again, as shown in Fig. 3.

The α_{12}/α_{34} ratio is closely related to the evolution of K_3 and K_1 with T. Close to T_{NS}, K_3 diverges with respect to K_1, as shown in the inset of Fig. 3(a), and thus, bend distortions become energetically prohibited. This forces **n** to align along great circles, which are the counterparts of straight lines on the sphere. In this configuration, schematically represented in Fig. 2(k), the four defects are necessarily located on a great circle. For shells homogeneous in thickness, all great-circle arrangements are degenerated in energy. However, this degeneracy is broken in our experimental shells that are heterogeneous in thickness. In this case, the ground state is achieved when the four defects are located on the equatorial plane, along the only great circle in which δ is uniform.

Far from T_{NS}, when $K_3 \approx K_1$, the four defects are confined at the thinnest part of the shell, as shown in Fig. 2(a). This results from the nonuniform thickness of these experimental shells [13]. Because of the nonvanishing thickness of the shells, the $+1/2$ defects are disclination lines that span the shell; to minimize their length, and thus the energy of the system, they group together at the thinner part of the shell. The approximate square arrangement of the defects comes from the approximate isotropy of the elastic constants at high temperatures. In fact, if $K_3/K_1 = 1$, the elastic energy associated with any director field is invariant under a $\frac{\pi}{2}$ rotation in **n**, converting bend distortions into splay distortions and vice versa. Therefore, the four defects must be located at the vertices of a square in their equilibrium configuration when $K_3/K_1 = 1$.

At intermediate temperatures, when $1 < K_3/K_1 < \infty$, the energy invariance under a $\frac{\pi}{2}$ rotation of **n** is broken, and thus, the four defects are necessarily arranged in a rhombus structure. Since K_1 does not change much in the temperature range studied, the motion of the defects is mainly controlled by the energy term associated to K_3. To explain why the distance between defects 1-2 becomes larger than the distance between defects 3-4 when K_3/K_1 increases, we investigate how increasing K_3 affects the equilibrium texture shown schematically in Fig. 2(h),

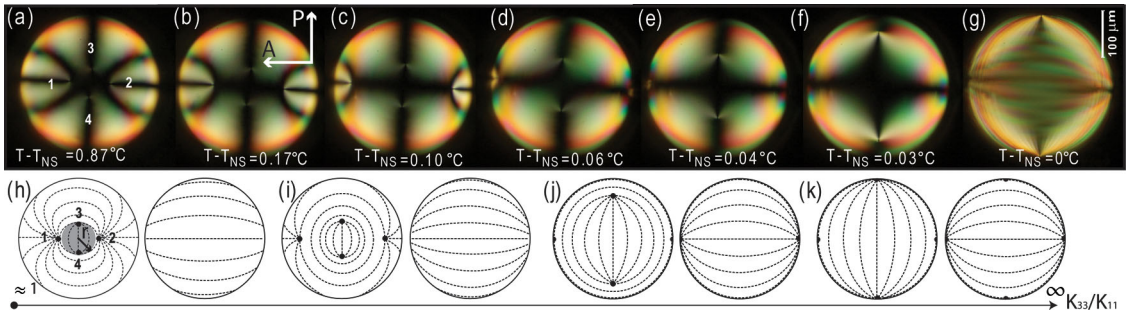

FIG. 2 (color online). (a)–(g) Cross-polarized images of an 8CB nematic shell as temperature T decreases toward the nematic-smectic phase transition temperature T_{NS}. (h)–(k) Evolution of the director field and defect structure during the process, in which K_3/K_1 changes between $1 < K_3/K_1 < \infty$. Each panel shows the director field on the lower (left) and upper (right) hemispheres.

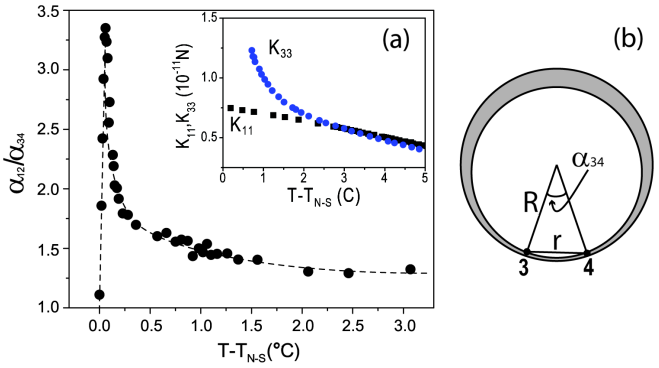

FIG. 3 (color online). (a) Ratio between the angular distances α_{12} (between defects 1-2) and α_{34} (between defects 3-4) as a function of $T - T_{NS}$. The inset shows the variation of K_3 and K_1 versus $T - T_{NS}$ [11]. (b) Geometric definition of α_{34}.

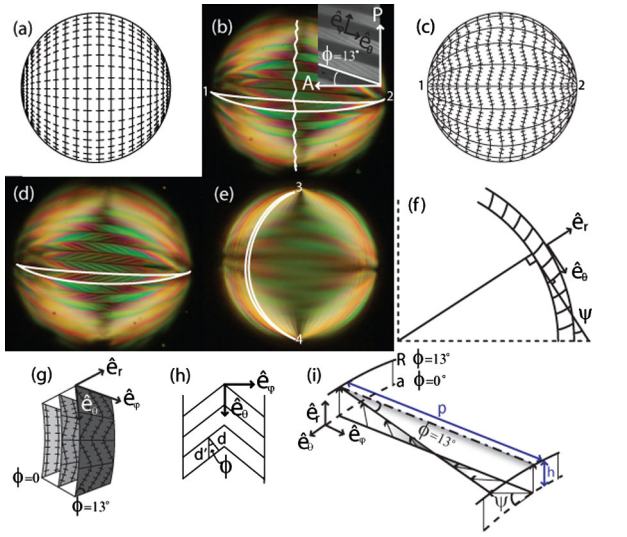

FIG. 4 (color online). (a) Longitudinal texture in a bidimensional smectic shell. The schematic shows the director field (horizontal discontinuous lines) and smectic layers (vertical continuous lines) on the upper hemisphere. (b) Birefringence texture observed in experimental smectic shells, where curvature walls divide each hemisphere in crescent domains. The inset in (b) shows that **n** is tilted in opposite directions in adjacent domains. (c) Director field corresponding to the texture shown in (b), where the walls provoke a zigzag modulation of the smectic layers. (e) Secondary curvature walls provoking a secondary optical modulation inside crescent domains. (d) Primary curvature walls at the thinner part of the shell. (f) Local three-dimensional smectic texture resulting from the bidimensional one shown in (a). (g) Possible three-dimensional texture in which the smectic layers twist through the shell thickness. (h) In this configuration, the effective layer thickness d' increases at the outer sphere compensating the effect of the different curvatures of the inner and outer spheres. (i) This texture implies a large tilt angle ψ with respect to the outer sphere normal.

where $K_3 \simeq K_1 \equiv K$. This nematic texture has a free energy that depends on K and the core energies of the defects. Now, we consider an increase of the bend constant from K to $K_3 = K + \Delta K_3$, while we keep the position of the defects fixed. The additional bend energy density, f_b, associated with this increase in the bend constant is mainly controlled by the radius of curvature of the director lines on the sphere. For a longitudinal director field such as the one shown in Fig. 2(k), f_b is zero since the integral curves of the director field are great circles, whereas $f_b = \Delta K_3 \cot^2\theta/2R^2$ for a latitudinal texture [14]. In Fig. 2(h), the curvature of the director lines is given by the locations of the defects, which allow us to split the sphere into two caps. In the lower cap, defined by the position of defects 3 and 4 [shaded region in Fig. 2(h)], the magnitude of f_b is given by $f_b^{(1)} \approx \Delta K_3 \cot^2(\alpha_{34}/2)/2R^2$, while for the remaining part of the sphere, $f_b^{(2)} \approx \Delta K_3 \cot^2(\alpha_{12}/2)/2R^2$. The corresponding energies, $F_b^{(1)}$ and $F_b^{(2)}$, can be respectively obtained as $F_b^{(1)} = f_b^{(1)} V^{(1)}$ and $F_b^{(2)} = f_b^{(2)} V^{(1)}$, where $V^{(1)}$ and $V^{(1)}$ are the volumes corresponding to the regions considered. In spherical coordinates, $V^{(1)} = \int_0^{\alpha_{34}/2} 2\pi R^2 h(1-\cos\theta)\sin\theta d\theta \approx \pi R^2 h \alpha_{34}^4/64$ and $V^{(2)} \approx 4\pi R^2 h$. In the limit of small angular distances, we obtain $F_b^{(1)} \approx \pi h \Delta K_3 \alpha_{34}^2/32$ and $F_b^{(2)} \approx 8\pi h \Delta K_3/\alpha_{12}^2$. The motion of the defects must be driven by the relaxation of this additional bent energy. Since $F_b^{(1)} \sim \alpha_{34}^2$ and $F_b^{(2)} \sim \alpha_{12}^{-2}$, the system will spontaneously increase α_{12} as K_3 increases, as we observe experimentally.

At T_{NS}, the shell becomes smectic. In the smectic phase, the molecules assemble in equispaced layers perpendicular to **n**. From a geometric point of view, the nematic texture shown in Fig. 2(k) can be readily converted into a simple smectic texture that preserves the four $s = +\frac{1}{2}$ defects [15]. The resulting smectic texture is schematically represented in Fig. 4(a), **n** is aligned along great circles and the bidimensional layers follow latitude lines. Experimentally, however, the texture develops a series of additional distinctive patterns in time. Just after the phase transition, a set of longitudinal lines form on the thicker part of the shell along the direction of the former director field, as shown in Fig. 4(b). These lines connect defects 1 and 2 and divide the shell into several crescent domains; one of those domains is highlighted in Fig. 4(b). As the sample is rotated between cross polarizers, the extinction angle periodically changes from $-13°$ to $+13°$ from one crescent domain to the next one, as shown in the inset of Fig. 4(b). Since **n** tilts in opposite symmetric directions in adjacent domains, the longitudinal lines can be identified as curvature walls [16]. We note that the resultant zigzag modulation of the smectic layers reminds us of the patterns observed after a Helfrich Hurault instability, as schematically indicated in Fig. 4(c).

After formation of these curvature walls, we observe that a secondary set of curvature walls form, but these have a much smaller angular distortion, $\approx 1°$, than the first. They extend across each domain perpendicularly to the tilted director field and give rise to a dark or light striped pattern

inside the domains, as shown in Fig. 4(d). The transition ends with the formation of primary curvature walls at the lower hemisphere, as shown in 4(e).

The description provided up to this point implicitly considers that **n** is uniform through the shell thickness, which is equivalent to a concentric stacking of the bidimensional structure of Fig. 4(c). Within this picture, the curvature walls would stem from the significant splay distortions in Fig. 4(a), which are released via the dilation of the layers at the walls [6]. Alternatively, the walls could result from the nonzero thickness of our experimental shells, as explained below.

In a thick shell, where the inner and outer spheres have significantly different radii, a strict planar anchoring can be satisfied on the inner sphere but not on the outer one; this results from the fact that having strong planar anchoring on a curved surface is only compatible with a bulk smectic texture without defects or layer dilations if the smectic layers grow outwardly from the convex side of the surface [15]. As a result, the smectic layers filling the shell are necessarily tilted at the outer surface violating the preferred planar anchoring and entailing an anchoring energy cost. To illustrate this, we construct a local bulk smectic texture from a surface texture with planar anchoring in Fig. 4(f); the result is a tilt angle, ψ, at the outer surface. For typical $R = 119$ μm and $h = 4$ μm, we obtain a typical tilt angle $\psi = \arccos(a/R) \approx 15°$.

It is tempting to think that this supplementary anchoring energy can be decreased if the smectic layer is progressively twisted from the inner sphere to the outer sphere in the way shown in Fig. 4(g). The twist angle is $\phi = 13°$ at the outer sphere and $\phi = 0$ at the inner sphere. Note that this twist implies a slight dilation of the layers via curvature walls. The zigzag of the smectic layers at the outer sphere implies that the layers are longer at the outer sphere than at the inner one; this corresponds to a larger effective layer separation, $d' = d/\cos\phi$, where d is the spontaneous thickness of the layer [see Fig. 4(h)]. The number of smectic layers on both surfaces is the same when $d'/d = R/a$ or equivalently when $\cos\phi = a/R$. For typical values of R and a, we obtain a twist angle at the outer surface of $\phi = 15°$, consistent with our experimental observations. Such an arrangement, however, also induces a tilt in the layers at the outer surface. Accommodating $\phi = 0$ at the inner surface and $\phi = 13°$ at the outer surface without layer dilation entails tilting the smectic layer by an angle ψ, with maximal value given by $\tan\psi = h/(p\tan\Phi)$, where p is the width of the corresponding crescent domain [see Fig. 4(i)]. Using the experimental values $p \approx 15$ μm, $\phi \approx 13°$, and $h \approx 4$ μm), we obtain $\psi = 45°$, implying there is also an important penalty in anchoring energy in the case of the considered twisted structure. Detailed energy calculations are required in order to elucidate the ultimate origin of the observed curvature walls.

Nematic shells undergo significant configurational changes as K_3/K_1 is varied. When $K_3/K_1 \approx 1$, the four $s = +\frac{1}{2}$ defects appear confined in the thinnest part of the shell, approximately located at the vertices of a square. By contrast, when $K_3/K_1 \gg 1$, the four defects relocate on the equatorial plane, confirming recent theoretical and simulation expectations [9,10]. The transition between these two limiting configurations proceeds continuously through a series of equilibrium states in which the defects typically arrange at the vertices of a rhombus. The ratio between the two diagonals depends on the value of K_3/K_1. This offers new possibilities for controlling the position of defects, and eventually, if these are functionalized, the directionality of the interactions between shells. New types of defects, not observed in shells before, appear when the nematic order is replaced by smectic order. At this point, we observe the formation of primary and secondary curvature walls, whose origins we have discussed by considering two possible scenarios. Our results open the way to rigorous theoretical calculations and exemplify the richness of behaviors that can be obtained when the elasticity of the material or the degree of order in the shell is changed.

T. L.-L. thanks the European Marie Curie Program (IEF-236091). A. F.-N. thanks the National Science Foundation (DMR-0847304).

*Teresa.Lopez-Leon@univ-montp2.fr

[1] N. D. Mermin, Rev. Mod. Phys. **51**, 591 (1979).
[2] M. Kleman and O. D. Lavrentovich, *Soft Matter Physics: An Introduction* (Springer-Verlag, New York, 2003).
[3] D. R. Nelson, Nano Lett. **2**, 1125 (2002).
[4] A. Arsenault *et al.*, J. Mater. Chem. **14**, 781 (2004).
[5] A. Fernandez-Nieves *et al.*, Phys. Rev. Lett. **99**, 157801 (2007).
[6] P. G. de Gennes and J. Prost, *The Physics of Liquid Crystals* (Clarendon Press, Oxford, England, 1993).
[7] T. C. Lubensky and J. Prost, J. Phys. II (France) **2**, 371 (1992).
[8] H. Poincaré, J. Math. Pures Appl. **1**, 167 (1885).
[9] H. Shin, M. J. Bowick, and X. J. Xing, Phys. Rev. Lett. **101**, 037802 (2008).
[10] M. A. Bates, J. Chem. Phys. **128**, 104707 (2008).
[11] N. V. Madhusudana and R. Pratibha, Mol. Cryst. Liq. Cryst. **89**, 249 (1982).
[12] A. S. Utada *et al.*, Science **308**, 537 (2005).
[13] T. Lopez-Leon *et al.*, Nature Phys. **7**, 391 (2011).
[14] We use here the covariant approach to nematic elasticity developed in: V. Vitelli and D. R. Nelson, Phys. Rev. E **74**, 021711 (2006).
[15] C. Blanc and M. Kleman, Eur. Phys. J. E **4**, 241 (2001).
[16] C. Blanc and M. Kleman, Eur. Phys. J. B **10**, 53 (1999).